

PAPER • OPEN ACCESS

Magnetic configuration scans during divertor operation of Wendelstein 7-X




























To cite this article: T. Andreeva *et al* 2022 *Nucl. Fusion* **62** 026032

View the [article online](#) for updates and enhancements.

You may also like

- [Gas exhaust in the Wendelstein 7-X stellarator during the first divertor operation](#)
U. Wenzel, G. Schlisio, P. Drewelow et al.
- [Identification of fast ion wall loads in Wendelstein 7-X from thermographic measurements](#)
Mark J H Cornelissen, Samuel A Lazerson, Yu Gao et al.
- [Equilibrium effects on the structure of island divertor and its impact on the divertor heat flux distribution in Wendelstein 7-X](#)
S. Zhou, Y. Liang, A. Knieps et al.

Magnetic configuration scans during divertor operation of Wendelstein 7-X

T. Andreeva^{1,*} , J. Geiger¹ , A. Dinklage¹ , G. Wurden² , H. Thomsen¹ ,
K. Rahbarnia¹ , J.C. Schmitt³ , M. Hirsch¹ , G. Fuchert¹ ,
C. Nührenberg¹ , A. Alonso⁴ , C.D. Beidler¹ , M.N.A. Beurskens¹ ,
S. Bozhenkov¹ , R. Brakel¹ , C. Brandt¹ , V. Bykov¹ , M. Grahl¹ ,
O. Grulke¹ , C. Killer¹ , G. Kocsis⁵ , T. Klinger¹ , A. Krämer-Flecken⁶ ,
S. Lazerson¹ , M. Otte¹ , N. Pablant⁷ , J. Schilling¹ , T. Windisch¹ and
the W7-X Team^a

¹ Max-Planck-Institute for Plasma Physics, Wendelsteinstraße. 1, 17491 Greifswald, Germany

² Los Alamos National Laboratory, Los Alamos, NM, 87545, United States of America

³ Auburn University, Auburn, AL, United States of America

⁴ Laboratorio Nacional de Fusión, CIEMAT, 28040 Madrid, Spain

⁵ Centre for Energy Research, Budapest, Hungary

⁶ Institute for Climate and Energy Research – Plasma Physics, Forschungszentrum Jülich, 52425 Jülich, Germany

⁷ Princeton Plasma Physics Laboratory, Princeton NJ, 08543, United States of America

E-mail: tamara.andreeva@ipp.mpg.de

Received 24 August 2021, revised 14 November 2021

Accepted for publication 1 December 2021

Published 4 January 2022



CrossMark

Abstract

Wendelstein 7-X (W7-X) (Greifswald, Germany) is an advanced stellarator, which uses the modular coil concept to realize a magnetic configuration optimized for fusion-relevant plasma properties. The magnet system of the machine allows a variation of the rotational transform (iota) at the boundary. In the latest W7-X operational phase a dedicated configuration scan has been performed varying the rotational transform between magnetic configurations with $\text{iota} = 5/4$ and $\text{iota} = 5/5$ at the boundary. This paper presents an overview of the experiments and of the main results with respect to confinement and stability. The main observation is an increase of the plasma energy in several intermediate configurations of the scan when the 5/5-islands are close to the plasma boundary but still inside the last-closed-flux-surface. In addition, these configurations showed marked MHD-activity with a crashing behavior related to the 5/5-islands. The corresponding mode amplitude was correlated with the size of the internal 5/5 islands.

Keywords: stellarator, confinement, iota scan, configuration variation, magnetic islands, Wendelstein 7-X

(Some figures may appear in colour only in the online journal)

* Author to whom any correspondence should be addressed.

^a See Klinger *et al* 2019 (<https://doi.org/10.1088/1741-4326/ab03a7>) for the W7-X Team.



Original content from this work may be used under the terms of the [Creative Commons Attribution 4.0 licence](https://creativecommons.org/licenses/by/4.0/). Any further distribution of this work must maintain attribution to the author(s) and the title of the work, journal citation and DOI.

1. Introduction

Wendelstein 7-X (W7-X) is an advanced stellarator, which uses the modular coil concept to realize a magnetic configuration optimized for fusion-relevant plasma properties including MHD-equilibrium and -stability, small neoclassical transport at low collisionality, small bootstrap current and favorable fast particle confinement [1]. The machine began operation in December 2015 [2] at the Max Planck Institute for Plasma Physics, Greifswald, Germany, and in October 2018 it successfully finished the second experimental phase with an uncooled divertor, the so-called test-divertor-unit [3]. This phase was devoted to the exploration of divertor operation, of high-performance hydrogen discharges and to the verification of those optimization principles which are accessible within the experimental capabilities and engineering limits of the device at this early stage of operation. In particular, the required accuracy of the magnetic field has been demonstrated [4], along with a small and controllable bootstrap current [5] and a reduction of the neoclassical transport [6]. The basis for the achievements and ambitious objectives of the machine is the magnetic field structure. Varying the magnetic field systematically is therefore a salient approach for testing the physics design of W7-X.

The coil system of W7-X was designed to allow a flexible change of the magnetic configurations. For this purpose, the magnet system of the five-field-period machine consists of 50 non-planar (NPC) and 20 planar (PC) superconducting coils, which are arranged in five identical modules. One of them is shown in figure 1. Each machine module consists of two flip-symmetric (stellarator-symmetric) half-modules. One W7-X half-module comprises 5 types of independently powered NPCs and two types of independently powered PCs, which allows for the realization of a large diversity of magnetic configurations to maximize the machine's flexibility [7, 8]. In the so-called Standard configuration, where all the NPCs carry equal currents and there is no current in the PCs, the rotational transform is equal to unity at the plasma boundary. The latter is then defined by a chain of five magnetic islands, providing the magnetic topology for an island divertor. Such a divertor can also be realized by changing the PC currents in such a way that the rotational transform becomes $5/6$ or $5/4$ at the plasma edge, in which case a chain of 6 or 4 islands arises in the poloidal direction, respectively. The PCs can also be used to shift the plasma column inwards or outwards. Furthermore, the variation of the magnetic field in the toroidal direction can be controlled by varying the currents in the NPCs appropriately. In this way, the 'mirror ratio' of the maximum and minimum field strength can, for instance, be varied. For additional experimental flexibility there are also ten control coils (see figure 1), which allow one to change the width and poloidal phase of the boundary islands. A supplementary set of trim coils is available for field perturbation investigations and corrections [9].

Operation of low-shear stellarators in combination with edge islands, like W7-X, is often very sensitive to small changes in the rotational transform. In low-to-medium density experiments conducted at the predecessor experiment,

Wendelstein 7-AS (W7-AS), which was also a low-shear stellarator, small changes in iota near rational iota values could lead to significant variations of the plasma confinement [10]. These W7-AS experiments comprised limiter (when the plasma volume is restricted by the divertor plates, which intersect nested flux surfaces) and divertor (when divertor plates intersect magnetic islands forming the plasma boundary) plasma configurations. Similar confinement changes due to variations in the rotational transform were also observed in the low-shear device Heliotron-J [11]. Configuration scans in the latest W7-X operational campaign aimed to investigate whether such effects, as observed in W7-AS or Heliotron-J, also exist in W7-X. This paper reports first results of two systematic scans of magnetic field properties. The first scan changes the rotational transform at the boundary from the high-iota- to the standard-configuration, varying the boundary value of iota from $5/4$ to $5/5$, respectively, to explore its effect on confinement and stability. We will refer to this scan in the paper as high-to standard-iota (HSI) scan. The second scan uses as base configuration one of the HSI-scan with an internal $5/5$ -island and varies the island size, wherefore we refer to this scan as island-size (IS) scan. Previously, there was only a small configuration scan in the initial operation phase (called OP1.1) for integral commissioning of the device [12], which was highly limited in configuration space as well as in the range of the plasma performance parameters. The particular configuration variation for the HSI-scan was chosen since the high-iota magnetic configuration has an almost negligible value of the bootstrap current at low densities [5, 13]. Hence, it was easier to distinguish between various possible impacts on the confinement properties since the influence of the bootstrap current on the rotational transform can be kept negligible.

The paper is organized as follows. In section 2 the technical realization of the HSI-scan is described. Section 3 presents an overview of the observations with respect to confinement, which is followed by section 4 on mode observations and related experiments comprising also the IS-scan. Finally, section 5 summarizes the results and concludes the paper.

2. Technical realization of the HSI-scan

The high-iota configuration ($t_b = 5/4$) was the upper bound of the HSI-scan and the standard configuration ($t_b = 5/5$) was the lower bound. The high-iota magnetic configuration is specified by equal currents of approximately +14 kA per winding in each NPC (each having 108 windings) specifying a positive magnetic field direction and by negative, identical planar coil currents of approximately -10 kA per winding in each PC (each having 36 windings) (see table 1). The nominal Standard magnetic configuration is specified by identical currents of approximately 13 kA per winding in all NPCs and vanishing currents in the PCs. Each intermediate configuration of the HSI-scan is characterized by equal coil currents in the NPCs and by equal coil currents in the PCs, whose values are varied between the bounds discussed above.

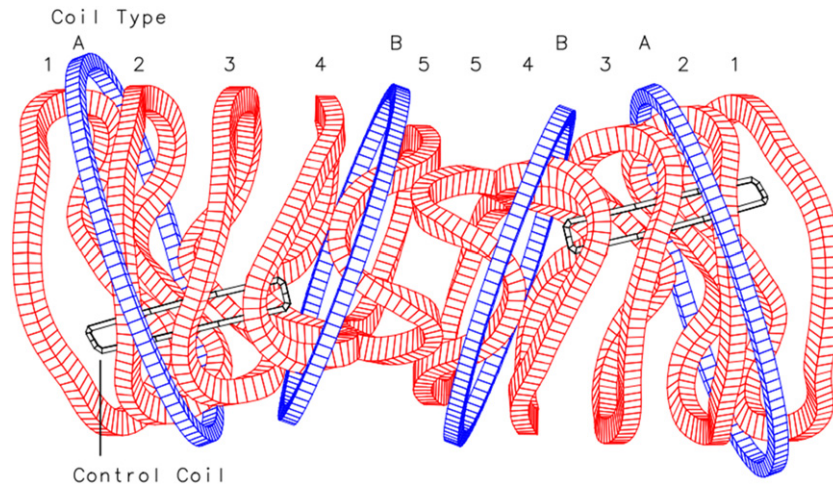


Figure 1. One field period of the W7-X coil system with modular (1 to 5, shown in red) and planar (A and B, shown in blue) coil types. Control coils are shown in black. © IOP Publishing. Reproduced with permission. All rights reserved.

Table 1. Characteristics of configurations in the iota scan: configuration labels used in the article, their experimental IDs, configuration names according to the W7-X internal specification, NPC and PC winding-currents in Ampere, coil current ratio PC/NPC, winding currents of the control coils, adjusted PC winding currents, rotational transform value in the center ι_0 and at the boundary ι_b and the volume in m^3 enclosed by LCMS of the vacuum configuration. Iota values ι_b are calculated from the field line tracing on the first good flux surface inside the boundary island chain. The experimental IDs of the discharges consist of the experiment day (yyyymmdd) being 20180927 and 20181017 for the HSI- and the IS-scan, respectively, and the experiment sequence numbers of the day given in column 2.

label Conf.	Exp.ID	W7-X config. name	NPC current (A)	PC current (A)	PC/NPC	CC current (A)	PC* current (A)	ι_0	ι_b	Volume (m^3)
A	HSI.09	FTM001	14 219	-10040	-0.706	0	-9873	1.015	1.211	25.64
B	HSI.15	FQM001	13 883	-7290	-0.525	0	-7032	0.966	1.167	31.22
C	HSI.16	FOM003	13 608	-5040	-0.370	0	-4707	0.926	1.100	31.45
D	HSI.17	FNM	13 577	-4790	-0.353	0	-4449	0.922	1.094	31.66
E	HSI.18	FNM001	13 546	-4540	-0.335	0	-4191	0.918	1.089	32.06
F	HSI.19	FNM002	13 515	-4290	-0.317	0	-3932	0.913	1.084	32.24
G	HSI.20	FMM	13 485	-4040	-0.300	0	-3674	0.910	1.078	32.41
H	HSI.21	FMM001	13 454	-3790	-0.282	0	-3416	0.906	1.069	31.92
I	HSI.22	FMM002	13 423	-3540	-0.264	0	-3158	0.902	1.066	32.61
J	HSI.28	FMM003	13 392	-3290	-0.246	0	-2899	0.899	1.061	32.61
K	HSI.29	FLM	13 361	-3040	-0.228	0	-2641	0.895	1.054	32.67
L	HSI.30	EJM	13 114	-1040	-0.079	0	-575	0.864	0.984	27.76
M	HSI.33	EJM004	13 016	-250	-0.019	0	242	0.853	0.984	30.46
N	IS.21	FMM002	13 423	-3540	-0.264	0	-3158	0.902	1.066	32.61
O	IS.22	FMM002	13 423	-3540	-0.264	-1745	-3158	0.902	1.066	32.61
P	IS.23	FMM002	13 423	-3540	-0.264	-1000	-3158	0.902	1.066	32.61
Q	IS.24	FMM002	13 423	-3540	-0.264	1000	-3158	0.902	1.066	32.61

The change in the rotational transform was produced by systematically varying the ratio of the PC-currents to the NPC-currents affecting boundary and central iota values in the same way. Table 1 shows an overview of the configurations and experimental IDs of the discharges in the HSI-scan as well as some technical information and configuration properties. Within this paper, the configurations of two experimental sessions (two scans) are discussed, which are labeled, for easier referencing, from **A** to **M** (HSI-scan) and from **N** to **Q** (IS-scan), respectively, as given in the table 1. The ratio of the current in the PCs to the current in the NPCs is the normalized figure of merit distinguishing the different configurations in the HSI-scan. It should be noted that the trim coils were

also used to compensate a 1/1-error field component intrinsic to the coil system due to unavoidable fabrication and assembly inaccuracies [14–17]. As these fields are thought to restore the ideal, periodic and stellarator-symmetric field to a good approximation, they are ignored for the MHD-equilibrium calculations.

As can be seen in table 1, the HSI-scan starts from configuration **A** (High-iota with the 5/4-islands at the plasma boundary) with two larger steps lowering the vacuum iota via configuration **B** to configuration **C**, followed by a sequence of configurations with smaller iota-steps up to configuration **K**. This scan ended with again a larger step with two closely related configurations **L** and **M** which are of the type of the

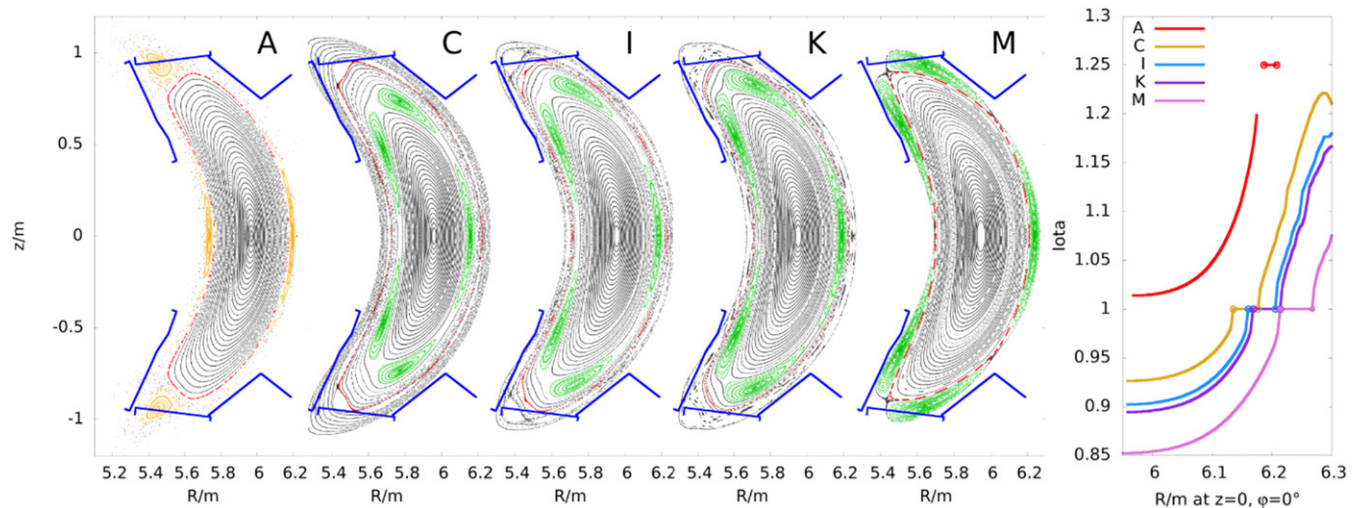


Figure 2. Left: Poincaré plots in the so-called bean-shaped poloidal plane (from vacuum field line tracing) showing the modification of magnetic flux surfaces for the subset of magnetic configurations: *A*, *C*, *I*, *K*, *M*. The last-closed-magnetic-surface is indicated in red color, the divertor structures are shown in blue. The central (and boundary) rotational transform decreases from configuration *A* toward *M*. The 5/5-islands of the configurations are highlighted in green. The 5/5 island chain appearing within the LCMS is seen in configuration *C* and moves outward in configurations *I* and *K*, and forms the boundary islands in configuration *M*. Configuration *I* is the base configuration used for the IS-scan. The edge island chain in configuration *A* is the 5/4 island highlighted in yellow. Right: rotational transform profiles for the shown subset of magnetic configurations in the same toroidal location along the major radius at $z = 0$. The gap in the iota-profile of configuration *A* is due to the stochastic region between LCMS and island surfaces.

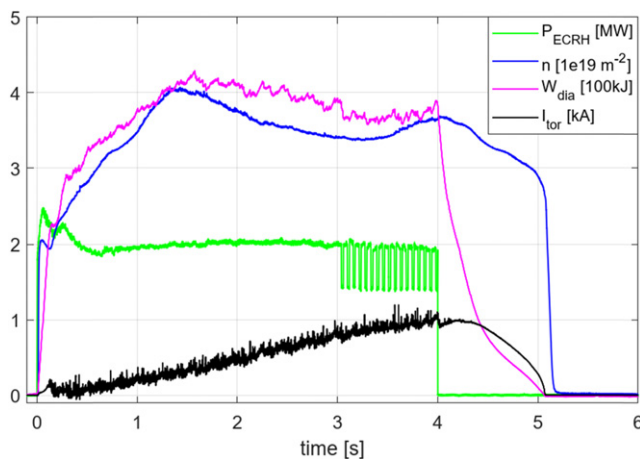


Figure 3. Typical time traces of plasma parameters during the configuration scan HSI, here for configuration *G*.

Standard configuration. Figure 2 shows the Poincaré plots and rotational transform profiles of the vacuum magnetic configurations for the end points of the HSI-scan (*A* and *M*), the end points of the finer scan (*C* and *K*) and the one configuration (*I*) inbetween which served as base configuration for the second scan (IS-scan). The iota-profiles are plotted along the major radius ($z = 0$) in the same plane as the Poincaré-plots. In the course of the HSI-scan the 5/4-island chain moves outward beyond the divertor structures due to the positive shear in iota ($d\iota/dr > 0$), which leads to limiter configurations. Simultaneously, the 5/5-resonance appears at the magnetic axis and moves outward due to the positive $d\iota/dr$. The last configurations *L* and *M* thus have the 5/5-islands at the boundary. The different radial locations of the islands of the 5/5-resonances

are visible in figure 2 in the configurations *C–M*. Configurations *I* and *K* show that in this range of the HSI-scan the 5/5-islands are rather close to the boundary, but they are still enclosed by the LCMS and, hence, stay within the confinement region.

For a comprehensive comparison of the configurations in this scan, it was intended to achieve identical experimental conditions for all of them. The ECRH power [18] and the line-integrated electron density, measured by interferometry [19], were targeted at $P_{\text{ECRH}} = 2$ MW and $\int n_e dl = 3.5 \times 10^{19} \text{ m}^{-2}$, respectively. The typical plasma heating duration was 4 s aiming at the formation of constant profiles given that the energy confinement times were in the range of 150–200 ms. Additionally, power modulation was applied in the last second of the discharges to enable heat pulse studies [20]. Figure 3 shows typical time traces of a discharge (*G*) in the HSI-scan. Although there is some temporal variation in the line-integrated density, most discharges showed a similar behavior. The coil currents for each configuration in this scan were adjusted to have a vacuum field strength on axis of about 2.52 T in the ECRH-launching plane (bean-shaped plane at $\varphi = 0^\circ$ as shown in figure 2) for proper central X2-heating with the 140 GHz gyrotrons.

3. Plasma confinement evaluation during HSI-scan

The main parameter used for characterizing the plasma confinement during the HSI-scan is the diamagnetic energy [21]. Figure 4 shows the time traces of the measured diamagnetic energy (figure 4(a)) and the ones of the electron line density (figure 4(b)) for a subset of experimental programs of this

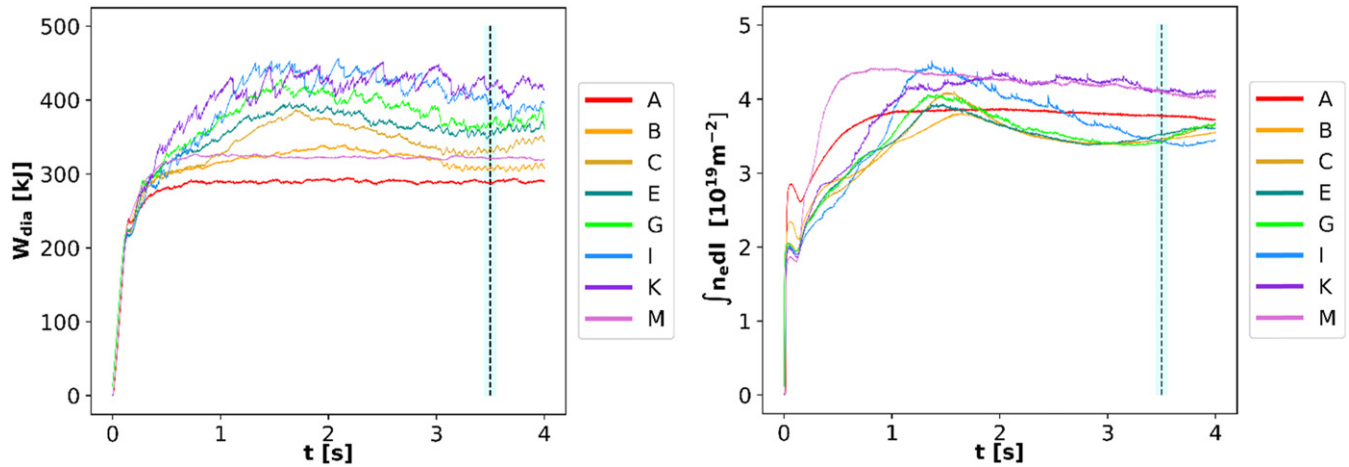


Figure 4. Diamagnetic energy and electron density of a subset of configurations of the HSI-scan. The vertical dashed line marks the time point for V3FIT, confinement and profile evaluations.

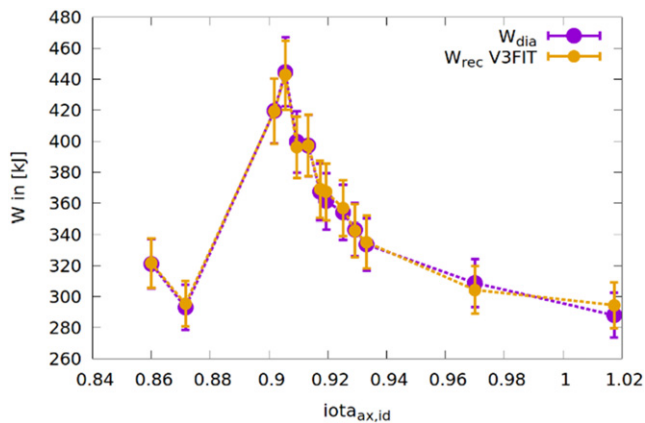


Figure 5. Measured diamagnetic energy (violet) with errorbars of $\pm 5\%$ (vertical lines) and reconstructed kinetic energy from V3FIT (orange), also with errorbars of $\pm 5\%$. Dashed lines connecting the experimental points are to guide the eye.

scan. An immediate observation from figure 4(a) is that, starting with configuration *A*, the diamagnetic energy increases as the vacuum-iota of the configurations is lowered, leading to the time trace with the largest energies measured in the shown subset, i.e. in configuration *K*. Experiment *M* (in the configuration of the standard-type) shows again smaller energy values. The line density signals display a rather similar behavior for most experiments (*B* to *G*) and also experiment *I* reaches the targeted line density value in the last second of the discharge. The experiments *A*, *K* and *M* show deviations in the line density values which will be discussed further below. Figure 5 presents the values of the diamagnetic energy versus the central ι value of the configurations for all experiments in this scan at the time point of 3.5 s, which is, as can be seen in figure 4(b), the time point where most line density traces cross the target line density value. At this time, the plasma profiles can well be assumed to be equilibrated. Figure 5 shows also the energy values resulting from an equilibrium reconstruction with the V3FIT-code [22] at 3.5 s using only the magnetic diagnostics without the diamagnetic signals providing thus an independent

plasma energy evaluation. The magnetic signals used in the V3FIT-reconstruction comprises both the segmented and the full Rogowski coils as well as the saddle loops [23]. The V3FIT-calculations (as well as the vacuum field evaluations of the volume and the rotational transform in this paper) used the CAD-coil geometries and adjusted planar coil currents (PC*), the latter are shown in table 1 [24]. The adjustments of the PC currents were performed to compensate for the iota-effect due to the elastic coil deformations caused by the electro-magnetic forces in the as-built coil geometries in order to restore the as-designed magnetic fields [25]. The diamagnetic energy error bars in figure 5 can be estimated as $\pm 5\%$ of the measured value in all experiments [21] and the same relative error was used for the V3FIT-values. As seen in figure 5, both energy evaluations, W_{dia} and W_{recV3FIT} , agree very well.

There are two peculiarities hidden in the comparison of the plasma energies measured in the different magnetic configurations shown in figure 5. First, there is a change in the plasma volume connected with the change in the vacuum rotational transform, and second, due to additional experiments at other conditions, the line density was different in some iota-scan programs, in particular, for the experiments in configurations *J* and *K*. Both effects are summarized in figures 6(a) and (b), the latter accounting for them.

We first consider the volume change with iota. The dislocation of the boundary islands affects the volume enclosed by the limiting separatrix up to the point where good flux surfaces interact with the divertor as limiting structure. Configuration *A* (high-iota configuration) and configurations *L* and *M* (standard-configuration-like configurations) are proper divertor configurations and for those, a boundary-island separatrix defines the plasma volume, which is naturally smaller than the volume of the limiter configurations *B* to *K* (see figure 2). For the latter configurations, good flux surfaces extend up to the divertor structures and such configurations will, in principle, provide a larger volume. This explains the larger difference in volumes of configurations *A*, *L* and *M* when comparing their values to the ones of the limiter configurations *B* to *K*. Second, the high-iota configuration *A* has a stronger shaping in

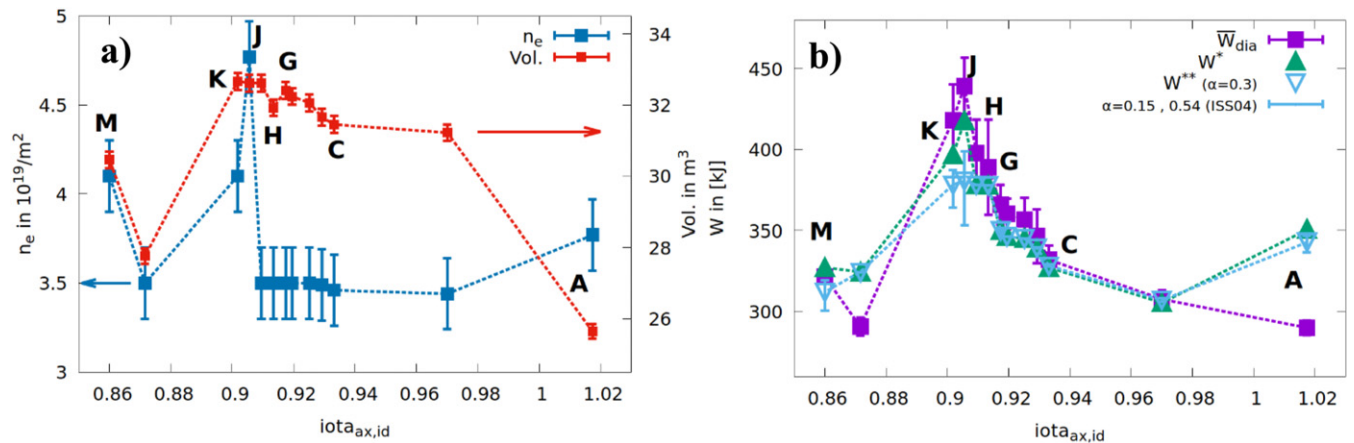


Figure 6. Configuration and experiment parameters displayed versus ι on axis making configuration labels (*A* to *M*) run sequentially from right to left. For orientation, some experimental points have been supplied with their label. Missing labels can be inferred from the indicated sequence. (a) Line-integrated density (@3.5 s) and volume of the vacuum configurations of the HSI-scan. The errorbar of $\pm 2 \times 10^{18} m^{-2}$ encompasses the statistical and systematic errors of the diagnostic [19]. The errorbar in the volume illustrates a variation in the minor radius $\delta r_{eff} = \pm 2$ mm where r_{eff} is in the range of 49 cm to 54 cm. (b) Measured diamagnetic energy W_{dia} @3.5 s (violet), energy W^* which is scaled to a norm-volume of $31.5 m^3$ (green filled triangles) and energy W^{**} which is additionally scaled to a norm-line-density of $3.5 \times 10^{19} m^{-2}$ (blue, open, upside-down triangles).

the sense that it is more slender than the standard configuration *M* (cf figure 2: horizontal extent of configurations *A* and *M*). This also affects their volumes (see table 1). In order to mitigate the effect of a changing volume—a larger volume with the same profiles on this volume results in a larger energy—the diamagnetic energy values were scaled to the same volume of $31.5 m^3$ using the volumes V_{Config} of the vacuum magnetic field (figure 6(a), red bullets), i.e. $W^* = W_{dia} \cdot (31.5 m^3 / V_{Config})$, which is shown in figure 6(b) as green triangles. The most marked changes are for the separatrix-configuration *A* and *L*, while for the configurations of the fine scan in ι (*C* to *K*) there is only a rather gradual correction of at maximum 5%. The general form of the energy- ι -dependence stays the same.

A more subtle effect results from the variations in the experimental conditions: the input power and the line-averaged electron density. The ECRH input power could be controlled quite accurately, while density control was much more difficult to achieve. Although a line density of $3.5 \times 10^{19} m^{-2}$ has been aimed at, there was a variation during the discharges (see figure 4(b)) and, due to additional experiments in configuration *I*, the experiments in configuration *J* and *K* showed deviating line densities of 4.7 and $4.1 \times 10^{19} m^{-2}$, respectively (figure 6(a)). Similar deviations due to interspersed experiments affected the line density of the experiment in configuration *M* in comparison to experiment *L*. The influence of the line density on confinement has been captured in scaling laws. However, for W7-X the dependence of the confinement on the density is not clear yet. To mitigate this effect here, a power dependence of the confinement time $\tau_E \sim n_e^\alpha$ is assumed, and the range of the exponent α is varied in order to provide a potential range of density-corrected energy values. We distinguish between a strong density dependence with $\alpha = 0.54$, the value taken from the ISS04-scaling law [26], a weak dependence with $\alpha = 0.15$, and a moderate dependence with a value in between, i.e. $\alpha = 0.3$.

The energy value scaled to the norm-volume (W^*) is further scaled to a norm line-density of $3.5 \times 10^{19} m^{-2}$, i.e. $W^{**} = W^* \cdot 3.5 \times 10^{19} m^{-2} / n_{e,exp}$. Here, $n_{e,exp}$ are the values at 3.5 s in the discharges which are displayed in figure 6(a). The light-blue reversed open triangles in figure 6(b) show the effect of the moderate density dependence and the ‘error bars’ indicate the deviation of a weak dependence (higher energy values) or a stronger (smaller energy values), which affects mainly the energy values of the experiments *A*, *J*, *K* and *M*. In particular, the experiments with the highest energy values (*J* and *K*) are corrected to result in energy values similar to the ones in configuration *H* and *I*. With these corrections the energy- ι curve still shows a steady but moderate increase from configuration *C* to *G*, then a stronger increase of about 10% from *G* to *H* from which a range of configurations (*H* to *K*) with higher confinement seems to reside.

Beyond the global confinement discussed so far, the question arises whether the increase in the stored plasma energy can also be seen locally, i.e. in the profiles measured by plasma diagnostics. For the purpose of discussing this, figure 7 shows for a selection of experiments with the same line densities (*A*, *C*, *E*, *G*, *I* and *M*) the profiles of ι of the respective vacuum configurations (VMEC-calculations [27] are used here), the fits [28] to the profiles of the total pressure, and the fits to the electron temperature and electron density from Thomson scattering (TS) [29]. The ion pressure part included in the total pressure is derived from ion temperature measurements by the XICS-diagnostic [30] and from a line-integrated value of Z_{eff} [31]. A notable hump is seen in the temperature and in the pressure figure in the outer third of the profiles for the configurations *G* and *I*. The pressure shows this more prominently. This increase in the profiles seems to be connected with the location of the $\iota = 5/5$ resonance in the ι -profile shown in figure 7 (top) which coincides with the location of increasing gradients. In order to show that this is not an artifact of

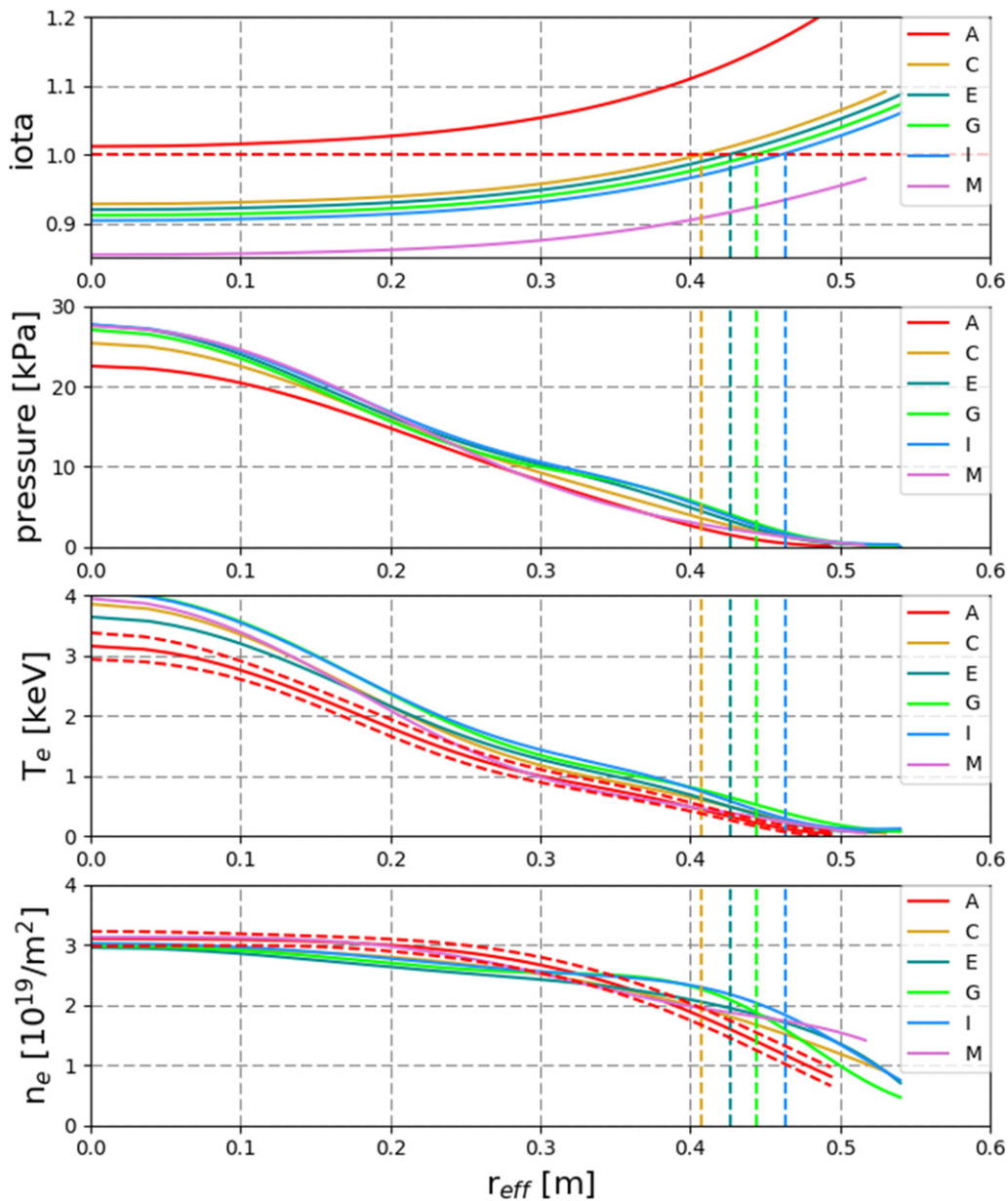


Figure 7. Radial plots versus effective minor radius in meter for the subset of configurations *A*, *C*, *E*, *G*, *I*, *M*, where the curve end indicates the position of the LCMS used in the VMEC-calculations underlying the profile evaluations: (a) rotational transform profiles; the red horizontal dashed line shows $\iota = 5/5$ and the vertical dashed lines mark the location of the $\iota = 1$ resonance for cases *C*, *E*, *G* and *I*; (b) fits to the total pressure; (c) fits to electron temperature from TS-data with typical error range shown by red dashed lines for the configuration *A*; (d) fits to line-integrated electron density from TS-data with typical error range shown by red dashed lines for the configuration *A*.

the fits, figure 8 shows the raw (not fitted) temperature profiles versus the major radius coordinate of the TS measurement line for a selection of configurations from the scan (same as in figure 7). This shows also a growth of the temperature data in the outer third of the profiles as the vacuum iota value is lowered. As pointed out before, the increase in the temperature data is connected with the position of the 5/5-islands. Therefore, the location and width of the 5/5-islands along the TS line-of-sight is marked for configuration *C* and *I* in figure 8 on the x -axis. Note, that the islands cannot be resolved by the TS-system because of an insufficient space resolution and because the measurement line of TS passes rather close to the x -point of the 5/5-islands and not through the o -point. This is also the

reason that an expected flattening of the temperature profile in the island region, caused by the high parallel heat conductivity, cannot be observed in the real-space profiles and is thus also not present in the fits to the profiles in figure 7.

To exclude an influence of the mapping on the evaluation results for the fitted data a sensitivity analysis of the pressure profile mapping was performed. Usually pre-calculated VMEC-equilibria (with assumed pressure profiles or vacuum configurations) are used to map raw experimental density and temperature data along the line-of-sight to the magnetic surfaces in order to obtain radial profiles. Sensitivity studies have been performed for the mapping of the experimental data with different finite-beta equilibria which confirmed that in the

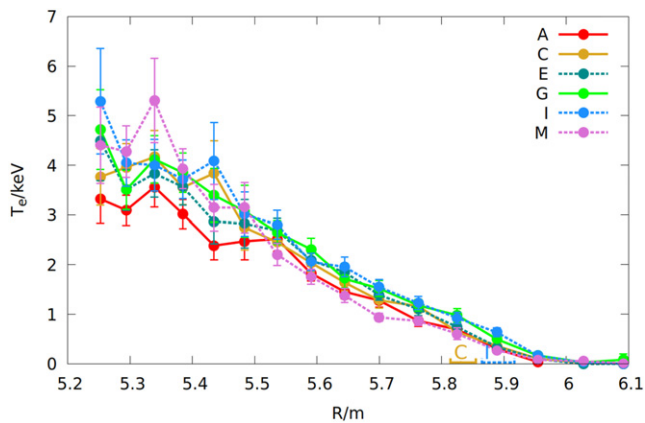


Figure 8. Raw (not fitted) electron temperature values as a function of the major radius along the line-of-sight of the TS-diagnostic for the subset of configurations *A*, *C*, *E*, *G*, *I* and *M*. The position and extent along the TS-line-of-sight of the 5/5-island in the vacuum magnetic field is marked on the horizontal axis for the two configurations *C* and *I*.

low-beta range (beta up to about 0.5%) there is little difference in the TS-mapping results due to different volume-averaged beta-values. Also, a variation of pressure shapes did not show significant effects on the TS-mapping.

4. Mode observations during configuration scans

Fluctuations and mode activity in the experiments of the HSI-scan have been monitored in various diagnostics with high temporal resolution, e.g. Mirnov-coils, segmented Rogowski coils, soft x-ray multi-camera-system, correlation reflectometry and visible radiation in video diagnostics. The characteristics of the fluctuations changes during the HSI-scan. Here, we focus on an irregular, low-frequency mode activity, which has been already observed and reported in reference [32]. In our HSI-scan, this mode activity has been mainly observed in the intermediate limiter configurations *C*–*K*, accompanying the increase in the diamagnetic energy (figure 9). This mode activity grows in intensity as the vacuum-iota is lowered and as the location of the 5/5-islands moves closer to the plasma boundary. It is strongest in the configurations *I* to *K*. The growth of this MHD-activity can be seen in figure 9 by noting that in configurations *B* to *L* there are power modulations present which can be easily identified in the configurations *B* to *E* and also in *L*. However, from configuration *F* onward to *K*, the power modulation in the diamagnetic signal is increasingly masked by superimposed crashing events which make the power modulation essentially invisible. This kind of mode activity is not present in the divertor configurations *A*, *L* and *M*, and in the first limiter configuration *B* of the HSI-scan which show a rather quiescent behavior.

We noted earlier that the internal 5/5-islands are in the outer portion of the confined-plasma region for the configurations *C* to *K* and that they are moving outward while steadily increasing their width. In [32] evidence has been provided by investigating soft-x-ray signals of the XMCTS diagnostic [33] that the crashing events are located in the regions of the 5/5-islands and have, therefore, been termed island-localized-modes (ILM). In order to test the influence of the island size on the confinement properties and the mode activity, specific experiments varying the island width were performed in a later experimental session with the discharges *N* to *Q* forming the IS-scan (see table 1). Here, different control coil currents (I_{cc}) were used to change the island size in four different discharges: one with nominal island width (*N*), two with decreased (*O*, *P*) and one with increased island width (*Q*). Poloidal and radial island position in these four discharges stayed the same. Figure 10 shows Poincaré plots of the region of the upper x -point of the 5/5-islands together with the divertor structure in the $\varphi = 0^\circ$ -plane for configurations *N*, *O*, *P* and *Q*. The variation of the island size can be clearly seen comparing configuration *O*, having the smallest island size, and *Q*—with the largest island size in this sequence. Note, the control coils do not only affect the 5/5-islands, but also the higher-order rationals further out. Because the magnetic field spectrum of the control coils also has high harmonics, increasing the currents in the control coils leads to an increase of the size of these high-order islands resulting in stochasticization of these regions by island overlapping. This occurs for both polarities. However, the polarity of the control coil currents for increasing the 5/5-islands seems to preserve more good flux surfaces outside the 5/5-islands than in the case of the polarity for decreasing the 5/5-islands size. In the latter case, the high-order island chains between the 5/5- and the 10/9-islands grow and lead to ergodic regions. It should be mentioned that finite-beta is known to increase the 5/5-island size so that the effect in a finite-beta plasma needs to be studied with appropriate MHD-equilibrium calculations with codes like, e.g. HINT [34], but this is beyond the scope of this paper.

The discharge conditions for the IS-scan (*N* to *Q*) were targeted to be the same as in the previous HSI-scan (*A* to *K*) with a heating power of $P_{ECRH} = 2$ MW, however, the line-integrated density $\int n_e dl$ had to be accepted with values in the range of 6 – $6.5 \times 10^{19} \text{ m}^{-2}$, due to the device conditions caused by the experimental program of this day in which this small scan was embedded. The NPC and PC currents of configurations *N* to *Q* correspond to the ones of the original configuration *I* and are provided in table 1 together with the currents of the control coils. Figure 11 shows the time traces of the diamagnetic energy for all four configurations. An inset displays part of the time traces with different offsets to better distinguish the different time behavior of the four time traces. The average value of the diamagnetic energy evaluated in the range of 3 to

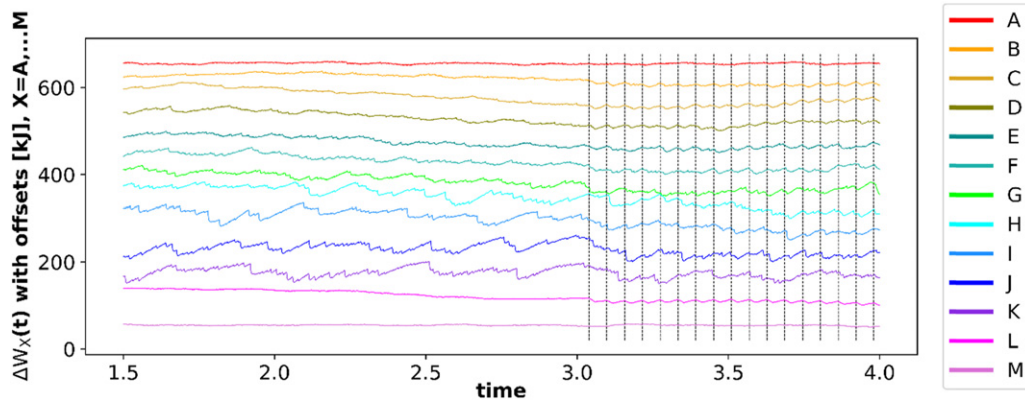


Figure 9. Oscillations visible in the diamagnetic energy signal in the different configurations of the HSI-scan. A varying offset has been added to the individual diamagnetic signals to separate them and to show them in sequential order (ordered by iota from top to bottom) in one plot. The scaling of the signals has been kept the same for all. The dashed vertical lines in the time range from 3 s to 4 s indicate the step-down time points of the power modulation applied in experiments *B* to *L*.

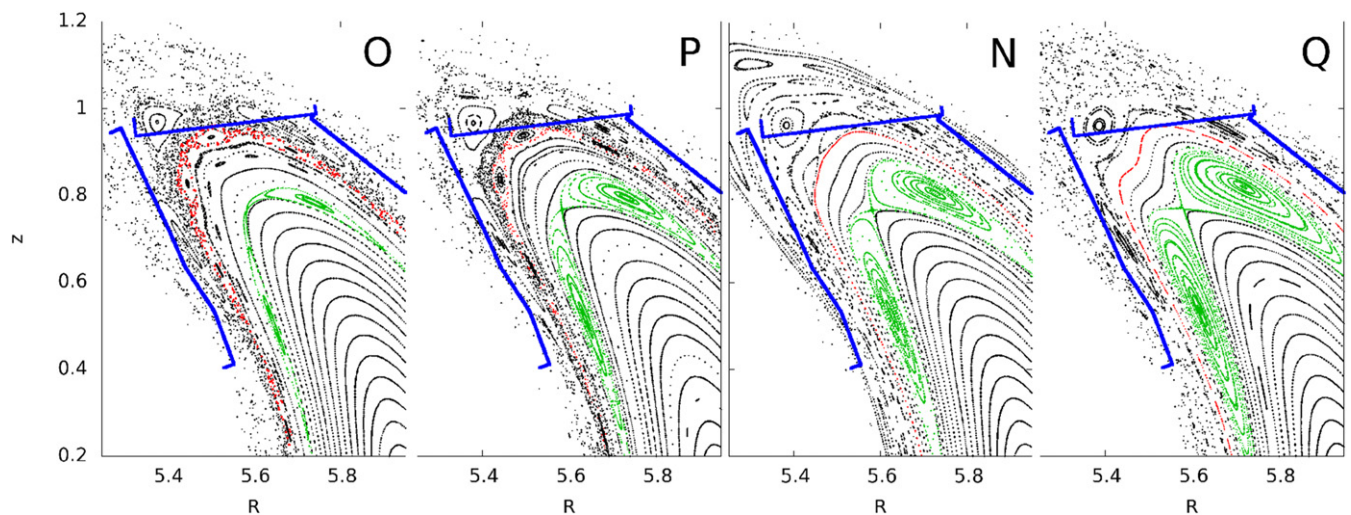


Figure 10. Poincaré plots reflecting the change of the magnetic topology in configurations *O* ($I_{cc} = -1.745$ kA, strongly reduced island size), *P* ($I_{cc} = -1$ kA, reduced island size), *N* ($I_{cc} = 0$ kA, reference) and *Q* ($I_{cc} = +1$ kA, increased island size) showing the different sizes of the 5/5-islands.

4 s shown in figure 11 stayed in these four experiments of the IS-scan almost at the same level independently of the island size. The small differences in the absolute diamagnetic energy values are most probably caused by the small changes of the line-integrated electron density (see table 2). At the same time the mode activity showed significant differences in the four discharges. Generally, the activity increased markedly with increasing island size being strongest in configuration *Q* with enlarged island size, while the activity was less prominent and less frequent in the configuration *P* with decreased island size and seemingly vanished in configuration *O*. The regular occur-

sions in the diamagnetic energy time trace seen in the latter configuration results from NBI-blips [35] of 20 ms duration every 200 ms for ion temperature measurements with active CXRS [36]. They have been marked in figure 11 for better visibility. Such NBI-blips were not present in the experiments in configuration *N* and *P*, but were applied in configuration *Q* and have, therefore, also been marked in figure 11. However, the MHD-activity with its irregular time behavior and strength renders the NBI-blips to invisible in the time trace of W_{dia} . Similar changes in the mode activity were detected also by other diagnostics.

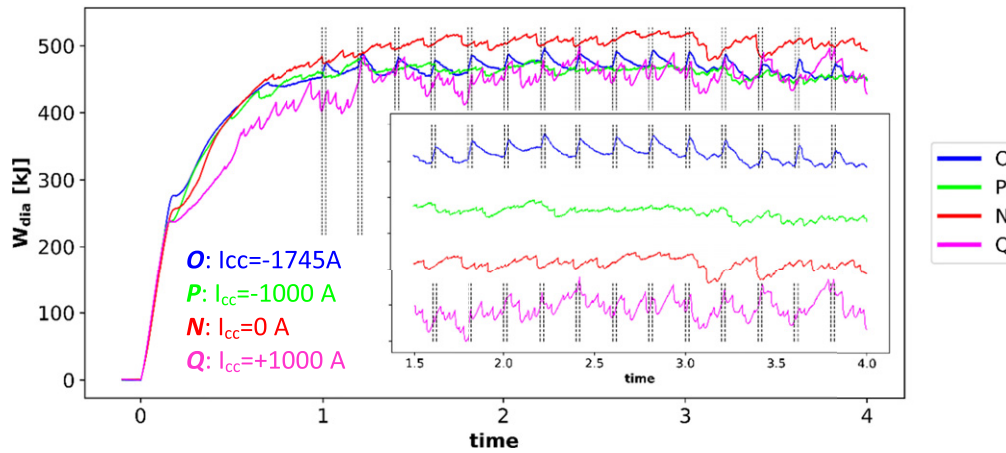


Figure 11. Time traces of the diamagnetic energy of the first 4 s of discharges N to Q using the same main vacuum field as configuration I , but varying the 5/5-island width using the control coils. The mode activity appears to depend on the island size as the energy signal variations become more intense for increasing island size (configuration Q) and are seemingly smoother for smaller island size. This is shown more prominently in the inset where the diamagnetic energy signals are separated by different offsets. The dashed vertical lines in both pictures indicate the time points and duration of the NBI-blips present in the experiments in configurations O and Q .

Table 2. Diamagnetic energy, line-integrated electron density and island size in the experiments N to Q . The reference configuration N has the same NPC and PC coil currents as configuration I of the HSI-scan.

Conf.	$\langle W_{\text{dia}} \rangle$ (kJ)	$\int n_e dl$ ($10^{19}/\text{m}^2$)	Island size	I_{cc} (A)
N	500	6.7	Reference	0
O	462	6.4	Strongly reduced	-1745
P	454	6.1	Reduced	-1000
Q	457	6.1	Increased	1000

5. Conclusions and outlook

In the latest W7-X divertor-operation experimental campaign, configuration scans (HSI and IS) were conducted exploring the magnetic configurations between the W7-X high-iota and standard-configuration by means of planar coil current change covering a range in central $\iota(0)$ from 0.854 to 1.012 corresponding to ι values at the boundary of 5/5 and 5/4, respectively. The HSI-scan consisted of a set of 13 experimental programs with very similar plasma parameters but a varied rotational transform. The rotational transform variation revealed an increase of the plasma energy and thus implicitly of the confinement time in the intermediate limiter configurations. The confinement improvement persists when accounting for effects of volume changes in the different configurations and when scaling the energy data to the same line density. The effect is also confirmed when comparing the profiles of the different experiments. A notable increase in the electron temperatures from TS-measurements is seen in the outer third of the plasma minor radius where the 5/5-islands reside. The reason for the confinement improvement is not yet clear although it is suggestive that it relates to the presence of the 5/5-islands close to the plasma boundary. It is known that islands can play an important role in building up radial electric fields affecting

plasma flow and turbulence and thus confinement [37]. First investigations in this direction have been started [38].

The confinement improvement is accompanied by ‘bursty’ MHD-activity being observed by several diagnostics in the intermediate limiter configurations. The mode, termed ILM, is related to the presence of the 5/5-island chain and its amplitude correlates with the size of the internal 5/5 islands: it becomes larger with island enlargement and decreases with the reduction of the island size. However, the change of the island size seems to have no effect on the diamagnetic energy which was shown in the IS-scan.

This first configuration scans in W7-X still leaves many questions open. Future experimental exploration of these ‘improved’ intermediate configurations is needed to further understand the reason for the confinement improvement and to explore the effect of higher beta values. Also, the profiles of plasma parameters and fluctuations across and around the islands need to be addressed further. One possibility would be to operate the control coils in a non-stellarator-symmetric mode. This allows to dislocate the 5/5-islands poloidally and allowing various diagnostics to access the o -point regions of the islands as well as the regions of the island x -points. This can contribute to a more complete insight into the effect of islands at the plasma boundary on plasma confinement.

Acknowledgments

This work has been carried out within the framework of the EUROfusion Consortium and has received funding from the Euratom research and training programme 2014–2018 and 2019–2020 under Grant Agreement Number 633053. The views and opinions expressed herein do not necessarily reflect those of the European Commission. US researchers are supported by the United States Department of Energy (U.S. D.o.E.), Office of Fusion Energy Sciences. PPPL research

was supported by U.S. D.o.E. Grant under Contract No. DE-AC02-09CH11466. Auburn research was supported by U.S. D.o.E. Grant DE-SC00014529. LANL research is supported by U.S. D. o.E./IPP collaboration under D.o.E. LANS Contract DE-AC52-06NA25396.

ORCID iDs

T. Andreeva  <https://orcid.org/0000-0003-2390-4240>
 J. Geiger  <https://orcid.org/0000-0003-4268-7480>
 A. Dinklage  <https://orcid.org/0000-0002-5815-8463>
 G. Wurden  <https://orcid.org/0000-0003-2991-1484>
 H. Thomsen  <https://orcid.org/0000-0002-6835-1494>
 K. Rahbarnia  <https://orcid.org/0000-0002-5550-1801>
 J.C. Schmitt  <https://orcid.org/0000-0002-9407-7636>
 M. Hirsch  <https://orcid.org/0000-0002-7120-6087>
 G. Fuchert  <https://orcid.org/0000-0002-6640-2139>
 C. Nührenberg  <https://orcid.org/0000-0002-3568-2035>
 A. Alonso  <https://orcid.org/0000-0001-6863-8578>
 C.D. Beidler  <https://orcid.org/0000-0002-4395-239X>
 M.N.A. Beurskens  <https://orcid.org/0000-0002-3354-0279>
 S. Bozhenkov  <https://orcid.org/0000-0003-4289-3532>
 C. Brandt  <https://orcid.org/0000-0002-5455-4629>
 V. Bykov  <https://orcid.org/0000-0003-3691-0631>
 M. Grahl  <https://orcid.org/0000-0003-0099-9224>
 C. Killer  <https://orcid.org/0000-0001-7747-3066>
 A. Krämer-Flecken  <https://orcid.org/0000-0003-4146-5085>
 S. Lazerson  <https://orcid.org/0000-0001-8002-0121>
 M. Otte  <https://orcid.org/0000-0003-3134-7579>
 N. Pablant  <https://orcid.org/0000-0001-6617-8459>
 J. Schilling  <https://orcid.org/0000-0002-6363-6554>

References

- [1] Grieger G. et al 1992 *Fusion Technol.* **21** 1767–78
- [2] Wolf R.C. et al 2017 *Nucl. Fusion* **57** 102020
- [3] Klinger T. et al 2019 *Nucl. Fusion* **59** 112004
- [4] Pedersen T.S., Otte M., Lazerson S., Helander P., Bozhenkov S., Biedermann C., Klinger T., Wolf R.C. and Bosch H.-S. 2017 Erratum: confirmation of the topology of the Wendelstein 7-X magnetic field to better than 1:100,000 *Nat. Commun.* **8** 14491
- [5] Neuner U. et al 2021 *Nucl. Fusion* **61** 036024
- [6] Beidler C.D. et al 2021 *Nature* **596** 221–6
- [7] Geiger J., Beidler C.D., Feng Y., Maaßberg H., Marushchenko N.B. and Turkin Y. 2015 *Plasma Phys. Control. Fusion* **57** 014004
- [8] Andreeva T. et al 2002 *Probl. At. Sci. Technol.* **4** 45–7
- [9] Bozhenkov S.A., Otte M., Biedermann C., Jakubowski M., Lazerson S.A., Sunn Pedersen T. and Wolf R.C. 2019 *Nucl. Fusion* **59** 026004
- [10] Hirsch M. et al 2008 *Plasma Phys. Control. Fusion* **50** 053001
- [11] Sano F. et al 2005 *Nucl. Fusion* **45** 1557
- [12] Dinklage A. et al 2018 *Nat. Phys.* **14** 855–60
- [13] Andreeva T. et al 2019 *Fusion Eng. Des.* **146** 299–302
- [14] Andreeva T., Bräuer T., Bykov V., Egorov K., Endler M., Fellingner J., Kiblinger J., Köppen M. and Schauer F. 2015 *Nucl. Fusion* **55** 063025
- [15] Lazerson S.A. et al 2018 *Plasma Phys. Control. Fusion* **60** 124002
- [16] Lazerson S.A. et al 2019 *Nucl. Fusion* **59** 126004
- [17] Bykov V., Zhu J., Carls A., Ivashov I., Geiger J., Hein B., Bosch H.-S. and Wegener L. 2019 *Fusion Sci. Technol.* **75** 730–9
- [18] Wolf R.C. et al 2019 *Plasma Phys. Control. Fusion* **61** 014037
- [19] Brunner K.J. et al 2018 *J. Instrum.* **13** P09002
- [20] Hirsch M. et al 2019 *EPJ Web Conf.* **203** 03007
- [21] Rahbarnia K. et al 2018 *Nucl. Fusion* **58** 096010
- [22] Hanson J.D. et al 2013 *Nucl. Fusion* **53** 083016
- [23] Endler M. et al 2015 *Fusion Eng. Des.* **100** 468–94
- [24] Otte M. 2020 private communication
- [25] Andreeva T., Bozhenkov S., Bykov V., Endler M., Fellingner J., Geiger J., Grahl M., Klinger T. and Thomsen H. 2017 *Fusion Eng. Des.* **123** 129–32
- [26] Yamada H. et al 2005 *Nucl. Fusion* **45** 1684
- [27] Hirshman S.P., van RIJ W.I. and Merkel P. 1986 *Comput. Phys. Commun.* **43** 143–55
- [28] Chilenski M.A., Greenwald M., Marzouk Y., Howard N.T., White A.E., Rice J.E. and Walk J.R. 2015 *Nucl. Fusion* **55** 023012
- [29] Pasch E., Beurskens M.N.A., Bozhenkov S.A., Fuchert G. and Wolf R.C. 2018 *Rev. Sci. Instrum.* **89** 10C115
- [30] Pablant N.A., Bell R.E., Bitter M., Delgado-Aparicio L., Hill K.W., Lazerson S. and Morita S. 2014 *Rev. Sci. Instrum.* **85** 11E424
- [31] Pavone A. et al 2019 *J. Instrum.* **14** C10003
- [32] Wurden G. 2019 Structure of island localized modes in Wendelstein 7-X *Proc. 46th EPS Conf. Plasma Physics (EPS-2019)* (Milan, Italy) (<http://ocs.ciemat.es/EPS2019PAP/pdf/P2.1068.pdf>)
- [33] Brandt C. et al 2020 *Plasma Phys. Control. Fusion* **62** 035010
- [34] Suzuki Y., Nakajima N., Watanabe K., Nakamura Y. and Hayashi T. 2006 *Nucl. Fusion* **46** L19–24
- [35] McNeely P. et al 2020 *Fusion Eng. Des.* **161** 111997
- [36] Ford O. et al 2020 *Rev. Sci. Instrum.* **91** 023507
- [37] López-Bruna D. et al 2018 *Nucl. Fusion* **58** 106031
- [38] Estrada T. et al 2021 *Nucl. Fusion* **61** 096011